Smart Materials and Structures

PAPER • **OPEN ACCESS**

Customized broadband structural vibration control using piezoelectric shunt absorbers

To cite this article: Hangxing Li *et al* 2025 *Smart Mater. Struct.* **34** 115014

OPEN ACCESS
IOP Publishing
Smart Materials and Structures
Smart Mater. Struct. **34** (2025) 115014 (21pp)
https://doi.org/10.1088/1361-665X/ae190f

Customized broadband structural vibration control using piezoelectric shunt absorbers

Hangxing Li, Waion Wong and Li Cheng*

Department of Mechanical Engineering, The Hong Kong Polytechnic University, Hong Kong Special Administrative Region of China, People's Republic of China

E-mail: li.cheng@polyu.edu.hk

Received 30 June 2025, revised 20 September 2025
Accepted for publication 29 October 2025
Published 11 November 2025

Abstract

Piezoelectric (PZT) shunt absorbers have shown promise for the control of vibrating structures due to their appealing lightweight and tunable features. However, the complex coupling among multiple structural components including the PZT patches presents a significant challenge in achieving optimal design, which turns out to be tedious and computationally costly. In this study, based on the experimentally measured or numerically simulated vibration response of primary structures, casted in terms of extracted Excitation-Dependent Representative Basis, a novel design methodology is proposed to optimally design the parameters of a multi-degree-of-freedom shunt circuit over an arbitrarily given thin-walled structure to achieve pre-defined target vibration reduction. The proposed analysis framework alongside the corresponding simplified model greatly reduces the complexity of the dynamic analysis while still retaining the essential electromechanical interaction effects taking place inside the coupled system, thereby offering practical benefits for the design of the shunt absorbers. In particular, an inverse design method is proposed to achieve customized vibration control. The whole approach is shown to be computationally efficient, as the solutions can be directly derived from analytical expressions. The effectiveness of the proposed approach is verified through both numerical simulations and experiments.

Keywords: customized vibration control, inverse design strategy, coupling analysis, piezoelectric shunt absorbers

1. Introduction

The control of structural vibration and its sound radiation holds considerable practical significance across a wide range of engineering applications [1–3]. Among various passive vibration control techniques, piezoelectric (PZT) shunt absorbers have attracted considerable attention due to their appealing features like compactness, lightweight, and adaptability. However, the intricate electromechanical coupling within the system, together with the mutual interactions among shunt absorbers and the tuning of numerous parameters in the fully coupled system, render the design process highly complex and challenging.

Similar to conventional dynamic vibration absorbers (DVAs), analytical approaches based on H_2 and H_∞ optimization criteria have been widely employed to determine the optimal shunt absorber parameters using lumped-parameter

* Author to whom any correspondence should be addressed.

models [4]. This method requires the accurate identification of the primary system's parameters, which is not always possible in practice. As an alternative, data-driven methods have emerged, including machine learning strategies based on time-averaged root mean square (RMS) structural responses [5], and energy-based design strategies that aim to maximize the average electrical power dissipated by the shunt circuits [6]. However, when PZT patches are employed for flexural vibration suppression of thin-walled structures, the accuracy of the lumped-parameter models is often compromised, thereby hindering the accurate determination of optimal shunt parameters [7].

A more logical approach consists in considering the coupling effects, particularly when a multi-degree-of-freedom shunt circuit is deployed with PZT elements integrated into the structure for broadband vibration control. To address the analytical complexity associated with such coupled systems, several methodologies have been proposed for the optimal design of shunt absorbers. One strategy consists in incorporating an LC filter circuit for each degree of freedom within the shunt configuration, as an attempt to decouple different degrees of freedom. This method results in a system with minimal coupling between shunt absorbers, thus simplifying the design process [8–12]. As an alternative, correction methods for residual mode contributions [13, 14] and sequential tuning procedures [15] have been introduced to account for the coupling effects involved in the design. To alleviate the reliance on explicit system modeling and to cope with the need for real-time monitoring, recent studies have introduced self-tuning strategies that operate independently of sophisticated system identification [16]. Furthermore, a frequency-swept shunt absorber has been developed, with parameters designed to vary periodically within predefined ranges [17, 18]. This class of absorbers eliminates the need for manual fine-tuning and demonstrates strong robustness against operational condition variations of the primary structure.

PZT patches attached to the primary structure offer a useful means to achieve effective vibration control. Although adjusting the physical layout of PZT patches such as dimension or position is challenging, the use of electrical shunt circuit, to form the so-called shunt absorbers, provides the flexibility one would need for structural vibration control. The integration of multiple degrees of freedom into the shunt circuit for suppressing a single resonant peak in the primary structure was shown to enhance both vibration attenuation performance and robustness against parameter mismatches [19, 20]. Moreover, for the simultaneous suppression of multiple resonant responses, a multi-port impedance network was shown to outperform the conventional RLC resonant circuits [21, 22]. Additionally, incorporating nonlinear capacitive components into shunt absorbers [23, 24] or integrating negative capacitance circuits [25–27] has also been shown to further improve the vibration control effectiveness.

To suppress the resonant responses of multiple vibration modes in thin-walled structures, multiple PZT patches are typically required, with each individually tuned to target a specific mode [28]. However, this approach tends to result in a bulky and impractical configuration. As an alternative, multi-degree-of-freedom resonant shunt circuit has been proposed, allowing a single PZT patch to control multiple structural modes [29, 30]. To optimize the parameters of the shunt circuit, machine learning techniques [5, 31] can be employed to learn the system's input–output behaviors directly from vibration data, demonstrating strong application potential. However, such approaches require a large amount of high-quality, labeled experimental data, which is often difficult to obtain in practice. As an alternative, the system identification-based method allows for explicit characterization of the structural dynamics and provides a base model to guide the design of the shunt circuit. Nevertheless, achieving high-performance control using this method critically relies on accurate modeling, which is particularly challenging for structures with high modal overlap [7, 32]. To address this challenge, the present work introduces a model-free approach for extracting the resonant dynamics of the PZT structure within the vector space spanned by the so-called Excitation-Dependent Representative Basis (EDRB) [33, 34]. The salient feature of this method lies in its independence from system modeling, making it applicable to arbitrary thin-walled structures.

To this end, a generic structure equipped with a single PZT patch connected to a multi-degree-of-freedom resonant shunt is investigated. This way, a single PZT patch would serve as multiple shunt absorbers. The salient challenge associated with this system stems from the intricate electromechanical coupling of the PZT patch with the primary structure, as well as the mutual interactions among multiple shunts. To address these limitations and achieve pre-defined vibration suppression targets, a novel design methodology is proposed based on the EDRB, which can be readily extracted from the experimentally measured data on an arbitrary vibrating structure. Specifically, a coupling analysis framework, along with a corresponding simplified model, is introduced to reduce the complexity of the dynamic analysis while retaining the essential electromechanical interaction effects inside the coupled system, thereby streamlining the design of shunt absorbers. Furthermore, contrary to the common practice of relying on fixed or predefined capacitance values in conventional design approaches, we further propose an inverse design approach to enable customized vibration control without prior assumptions on circuit parameters.

The outline of this paper is as follows. Section 2 presents the theoretical framework and establishes the proposed methodology. Section 3 substantiates the proposed approach and demonstrates its efficacy in dealing with two typical cases. The first case involves a rectangular plate, where a stringent response control requirement is imposed to evaluate the efficacy of the proposed method. In the second case, a square plate is used to assess the suitability of the proposed method for systems with symmetric modes and its capability to achieve all-equal-peak response control.

Section 4 presents and discusses the results of the experimental validation, with the main conclusions summarized in section 5.

2. Theoretical formulation and design methodology

2.1. Coupled formulation of a PZT structure

Consider a generic thin-walled structure subjected to an external excitation force $\mathbf{F}_s(s)$. A PZT patch is attached to the structure and interfaced through a shunt circuit characterized by its electrical admittance $Y(s)$, as shown in figure 1.

Dynamic equation of the PZT structure can be derived from Hamilton's principle [35, 36] and cast into the following general form:

$$\begin{aligned} s^2\mathbf{M}_s\mathbf{X}(s)+\mathbf{K}_s\mathbf{X}(s)+\boldsymbol{\gamma}v(s)&=\mathbf{F}_s(s)\\ \boldsymbol{\gamma}^T\mathbf{X}(s)-Cv(s)&=q(s) \end{aligned} \tag{1}$$

where s denotes complex variable; $\mathbf{M}_s$ and $\mathbf{K}_s$ the mass and stiffness matrices of the coupled system, respectively; $\mathbf{X}(s)$ and $\mathbf{F}_s(s)$ the vectors of nodal displacement response and external force vectors, respectively; $\boldsymbol{\gamma}$ the PZT coupling vector; C the inherent capacitance of the PZT patch; $v(s)$ and $q(s)$ the voltage and charge boundary conditions of the PZT patch, respectively.

While this matrix equation can theoretically be decomposed in modal space, its accurate representation becomes increasingly difficult for complex structures. To overcome this challenge, this equation is projected into the subspace spanned by the EDRB, which can be derived from either experimentally measured or numerically simulated response data. The use of the EDRB was first introduced in [33] to address the challenges associated with closely spaced modes in a structure. In that work, the authors demonstrated the use of EDRB for optimizing a DVA, by following similar design procedure as the mode-based approaches. Subsequently, in [34], the authors mathematically proved that the singular vectors obtained through singular value decomposition (SVD) of measured structural responses are equivalent to the EDRB. Since the measured vibration response depends on both the structural dynamics of the primary structure and the spatial/temporal characteristics of the applied excitation, the resulting singular vectors obtained via SVD are inherently excitation-dependent. As a result, the acquired structural response can be decomposed as:

$$\mathbf{X}(s)=\mathbf{U}\boldsymbol{\Sigma}\mathbf{V}^H(s), \tag{2}$$

where matrices $\mathbf{U}$ and $\mathbf{V}$ contain the left and right singular vectors, corresponding to the spatial and frequency-domain information of the system response, respectively. The diagonal entries of the singular value matrix $\boldsymbol{\Sigma}$ represent the associated singular values, which are non-negative real numbers. The number of retained singular vectors is determined based on a cumulative energy criterion, *i.e.* only the smallest subset of dominant singular vectors is retained, such that the sum of their corresponding singular values exceeds 90% of the total sum of all singular values. Substituting equation (2) into equation (1) yields:

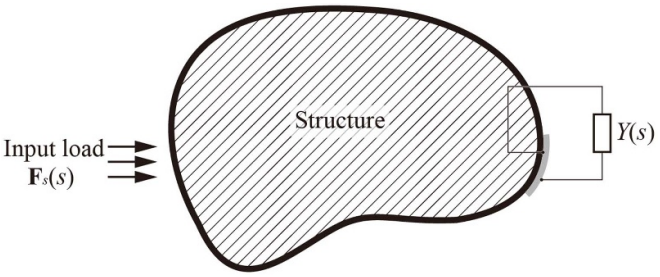

Figure 1. Schematic of a generic structure coupled with one piezoelectric patch.

$$\begin{aligned} s^2\mathbf{M}\boldsymbol{\eta}(s)+\mathbf{K}\boldsymbol{\eta}(s)+\boldsymbol{\theta}v(s)&=\mathbf{F}(s)\\ \boldsymbol{\theta}^{\mathrm{T}}\boldsymbol{\eta}(s)-Cv(s)&=q(s) \end{aligned} \tag{3}$$

where

$$\mathbf{M}=\mathbf{U}^{\mathrm{T}}\mathbf{M}_s\mathbf{U},\ \mathbf{K}=\mathbf{U}^{\mathrm{T}}\mathbf{K}_s\mathbf{U},\ \boldsymbol{\theta}=\mathbf{U}^{\mathrm{T}}\boldsymbol{\gamma},\ \boldsymbol{\eta}=\boldsymbol{\Sigma}\mathbf{V}^H. \tag{4}$$

According to Ohm's law,

$$q(s)=\frac{Y(s)}{s}v(s), \tag{5}$$

where $Y(s)$ denotes the admittance of a shunt circuit. Substitution of this equation into equation (3) gives

$$s^2\mathbf{M}\boldsymbol{\eta}(s)+\mathbf{K}\boldsymbol{\eta}(s)+\boldsymbol{\theta}v(s)=\mathbf{F}(s), \tag{6.a}$$

$$\boldsymbol{\theta}^{\mathrm{T}}\boldsymbol{\eta}(s)-\frac{1}{h(s)}v(s)=0, \tag{6.b}$$

where

$$h(s)=\frac{s}{Y(s)+sC}. \tag{7}$$

After substituting equations (6.b) into equation (6.a), the following expression is obtained:

$$\left[s^2\mathbf{M}+\mathbf{K}+h(s)\,\boldsymbol{\theta}\boldsymbol{\theta}^{\mathrm{T}}\right]\boldsymbol{\eta}(s)=\mathbf{F}(s). \tag{8}$$

In the above equation, structural matrix $\mathbf{Z}(s)=s^2\mathbf{M}+\mathbf{K}+h(s)\,\boldsymbol{\theta}\boldsymbol{\theta}^{\mathrm{T}}$ is non-diagonal, indicating the coupling among different EDRBs due to the electromechanical interaction introduced by the PZT patch. The presence of the off-diagonal terms introduces significant complexity in the design of the shunt absorber. Nevertheless, diagonalization of the structural matrix can be achieved through appropriate reformulation of

the governing equation. For example, equation (8) can be reformulated as:

$$\begin{bmatrix} \frac{\det[\mathbf{Z}(s)]}{\mathrm{adj}[\mathbf{Z}(s)]_{1,1}} & \cdots & 0 \\ \vdots & \ddots & \vdots \\ 0 & \cdots & \frac{\det[\mathbf{Z}(s)]}{\mathrm{adj}[\mathbf{Z}(s)]_{I,I}} \end{bmatrix} \boldsymbol{\eta}(s) = \begin{bmatrix} 1 & \cdots & \frac{\mathrm{adj}[\mathbf{Z}(s)]_{1,I}}{\mathrm{adj}[\mathbf{Z}(s)]_{1,1}} \\ \vdots & \ddots & \vdots \\ \frac{\mathrm{adj}[\mathbf{Z}(s)]_{I,1}}{\mathrm{adj}[\mathbf{Z}(s)]_{I,I}} & \cdots & 1 \end{bmatrix} \mathbf{F}(s), \tag{9}$$

where det $[\mathbf{Z}(s)]$ and adj $[\mathbf{Z}(s)]$ represent the determinant and the adjugate matrix of $\mathbf{Z}(s)$, respectively, with adj $[\mathbf{Z}(s)]_{i,j}$ $(i,j = 1,2,\ldots,I)$ denoting the element at the ith row and jth column. With the structural matrix now diagonalized, the transfer function of the coupled system can be derived as:

$$H_i(s) = \frac{\mathrm{adj}[\mathbf{Z}(s)]_{i,i}}{\det[\mathbf{Z}(s)]}. \tag{10}$$

To derive the analytical expression of equation (10), it is necessary to compute both the determinant of the structural matrix and the diagonal elements of its adjugate matrix. Specifically, the diagonal element adj $[\mathbf{Z}(s)]_{i,i}$ can be obtained by computing the determinant of the submatrix formed by removing the ith row and ith column from $\mathbf{Z}(s)$. According to the matrix determinant lemma [37, 38]:

$$\det\left(\mathbf{A}+\mathbf{u}\mathbf{v}^{\mathrm{T}}\right) = \det(\mathbf{A})\left(1+\mathbf{v}^{\mathrm{T}}\mathbf{A}^{-1}\mathbf{u}\right). \tag{11}$$

Using this equation, equation (10) writes

$$H_i(s) = \frac{1+h(s)\sum_{j=1,\,j\neq i}^{I}\frac{\vartheta_j^2}{s^2M_j+K_j}}{(s^2M_i+K_i)\left[1+h(s)\sum_{j=1}^{I}\frac{\vartheta_j^2}{s^2M_j+K_j}\right]}, \tag{12}$$

in which M_i and K_i represent the ith diagonal elements of matrices $\mathbf{M}$ and $\mathbf{K}$, respectively, and ϑ_j the jth element of vector $\boldsymbol{\Theta}$. It should be noted that, since the expression in equation (12) is explicit which relies only on scalar operations, the proposed approach remains numerically stable and scalable even for large EDRB bases.

2.2. Design methodology for shunt absorbers with coupling

The resonant shunt circuit with multiple degrees of freedom employed in this study is illustrated in figure 2.

Using equation (7), the transfer function of this resonant circuit is given by

$$h(s) = \frac{1}{C+\sum_{n=1}^{N}\frac{\omega_n^2 C}{s^2+2s\omega_n\xi_n+\omega_n^2\frac{C}{C_n}}}, \tag{13}$$

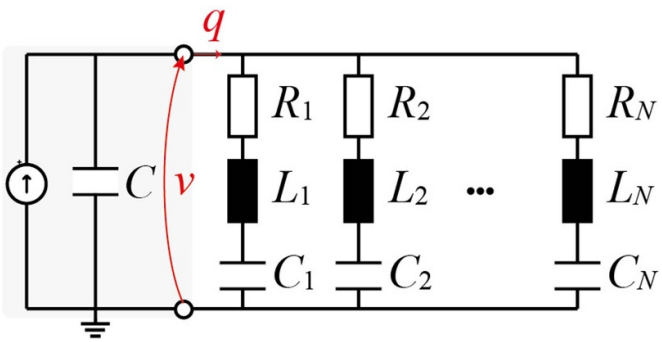

Figure 2. Schematic of the resonant shunt circuit with multiple degrees of freedom. C denotes the inherent capacitance of the piezoelectric patch, while R_n, L_n, and C_n represent the resistance, inductance, and capacitance of the nth branch, respectively.

where C_n denotes the capacitance of the nth branch in figure 2, and the frequency ω_n and damping ratio ξ_n are defined as

$$\omega_n = \sqrt{\frac{1}{L_nC}}, \xi_n = \frac{R_n}{2L_n\omega_n}, \tag{14}$$

in which R_n and L_n represent the resistance and inductance of the nth branch. Substituting equation (13) into equation (12) yields

$$H_i(s) = \frac{1}{s^2M_i+K_i+\frac{\vartheta_i^2}{C+\mathbb{C}_s+\mathbb{C}_p}\frac{s^2+2s\omega_n\xi_n+\omega_n^2\frac{C}{C_n}}{s^2+2s\omega_n\xi_n+\omega_n^2\left(\frac{C}{C_n}+\frac{C}{C+\mathbb{C}_s+\mathbb{C}_p}\right)}}, \tag{15}$$

where

$$\mathbb{C}_s = \sum_{m=1,\,m\neq n}^{N}\frac{\omega_m^2 C}{s^2+2s\omega_m\xi_m+\omega_m^2C/C_m}$$
$$\mathbb{C}_p = \sum_{j=1,\,j\neq i}^{I}\frac{\vartheta_j^2}{s^2M_j+K_j}. \tag{16}$$

In the above equations, $\mathbb{C}_s$ represents the contribution of the residual degrees of freedom of the shunt circuit $(m \neq n)$, while $\mathbb{C}_p$ reflects the influence of the residual degrees of freedom of the primary system $(j \neq i)$. Since both terms are frequency-dependent and involve unknown parameters ω_m and ξ_m, two assumptions are introduced to approximate these functions as known constants.

1) For a resonant structure, response around frequency $\Omega_i = \sqrt{\frac{K_i}{M_i}}$ (equation (15)) represents the transfer function of the ith EDRB, indicating that the response H_i should be analyzed around the resonant frequency Ω_i), which is far from the resonant frequency ω_m (residual degrees of freedom of the shunt circuit $(m \neq n)$) and $\Omega_j = \sqrt{\frac{K_j}{M_j}}$ (residual degrees of freedom of the primary system $(j \neq i)$), remains relatively flat (figure 3). This suggests that $\mathbb{C}_s$ and $\mathbb{C}_p$ in

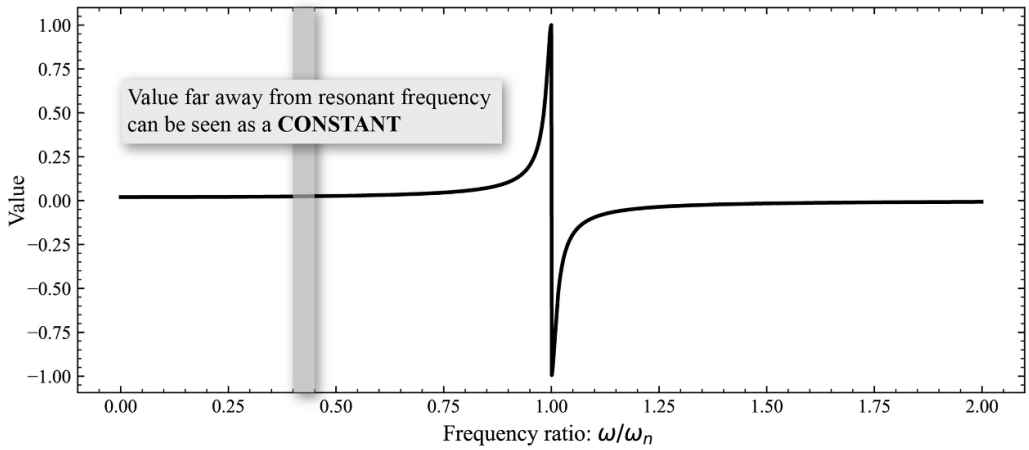

Figure 3. Dynamic response of resonant structure.

equation (16) can be approximated as constant by making $\omega = \Omega_i$.

Note this assumption applies to the EDRB instead of structural modes. The EDRB framework, originally developed in [33, 34], is particularly powerful to handle systems with closely spaced or overlapping structural modes. A key appealing feature is that even when multiple structural modes share nearly identical natural frequencies, their combined effect can be captured by a single dominant EDRB through SVD of the measured response data. This effectively 'merges' closely spaced dynamics into one EDRB, thereby avoiding the need to resolve them individually. Consequently, the resulting EDRBs typically exhibit well-separated peaks. This built-in filtering mechanism ensures that the final EDRB set satisfies the required separation for the approximation.

2) Additionally, when the equivalent stiffness ratio μ (as defined in equation (20)) of the absorber is much smaller than 1 (which is generally the case for resonant absorbers), the resonant frequency of the absorber should be very close to the targeted resonant frequency of the primary system, and the damping coefficient is usually small.

Taking these two assumptions (to be verified by subsequent analyses), i.e. $\omega_m^2\left(\frac{C}{C_m}+\frac{C}{C+\mathbb{C}_\mathrm{p}}\right)=\Omega_m^2, \xi_m = 0, s = j\Omega_i$, equation (16) can be approximated by

$$\mathbb{C}_\mathrm{s} = \sum_{m=1,m\neq n}^{N} \frac{\frac{\Omega_m^2}{C/C_m+\frac{C}{C+\mathbb{C}_\mathrm{p}}}C}{-\Omega_i^2+\frac{\Omega_m^2}{C/C_m+\frac{C}{C+\mathbb{C}_\mathrm{p}}}C/C_m}$$
$$\mathbb{C}_\mathrm{p} = \sum_{j=1,j\neq i}^{I} \frac{\vartheta_j^2}{-\Omega_i^2 M_j + K_j}. \tag{17}$$

Substituting equation (17) into equation (15), the residual degrees of freedom associated with both the shunt circuit and the primary system are eliminated, with their dynamic effects approximately preserved. This enables the complex PZT coupled system to be simplified as a two-degree-of-freedom mechanical system, as shown in figure 4.

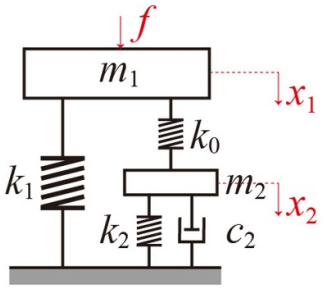

Figure 4. Equivalent mechanical model of piezoelectric structure.

The parameter mapping relationship between this equivalent mechanical model and the PZT structure is summarized as follows (see appendix A for more details),

$$m_1 = \frac{M_i}{\vartheta_i^2}, \quad k_1 = \frac{K_i}{\vartheta_i^2}, \quad k_0 = \frac{1}{C+\mathbb{C}_\mathrm{s}+\mathbb{C}_\mathrm{p}}$$
$$k_2 = \frac{1}{C_n}, \quad m_2 = L_n, \quad c_2 = R_n. \tag{18}$$

With the PZT structure approximated as a two-degree-of-freedom system, the fixed-point theory becomes applicable for the design of the shunt absorber. Accordingly, the normalized magnitude of equation (15) writes

$$H_i(s)K_i = \frac{-\lambda^2+\beta^2+2\lambda\gamma j\xi_n}{(-\lambda^2+\beta^2)(-\lambda^2+1)+\mu(-\lambda^2+\gamma^2 C/C_n)+2\lambda\gamma[-\lambda^2+1+\mu]j\xi_n}, \tag{19}$$

where

$$\lambda = \frac{\omega}{\Omega_i}, \gamma = \frac{\omega_n}{\Omega_i}, \beta = \frac{\omega_n}{\Omega_i}\sqrt{\frac{C}{C_n}+\frac{C}{C+\mathbb{C}_\mathrm{s}+\mathbb{C}_\mathrm{p}}},$$
$$\mu = \frac{\vartheta_i^2}{K_i(C+\mathbb{C}_\mathrm{s}+\mathbb{C}_\mathrm{p})}. \tag{20}$$

According to the fixed-point theory, the frequency response curve of equation (19) always passes through two invariant

points, p and q, regardless of ξ_n. These points can be determined by solving

$$\frac{-\lambda^2+\beta^2}{\left(-\lambda^2+\beta^2\right)\left(-\lambda^2+1\right)+\mu\left(-\lambda^2+\gamma^2 C/C_n\right)} = -\frac{1}{-\lambda^2+1+\mu}. \tag{21}$$

Solving this equation yields the expressions for the two fixed points, given by

$$\lambda_{p,q}^2 = \frac{1+\mu+\beta^2 \pm \sqrt{\left(1+\mu+\beta^2\right)^2 - 2\beta^2\left(2+\mu\right) - 2\mu\gamma^2\frac{C}{C_n}}}{2}. \tag{22}$$

The optimization procedure first equalizes the amplitudes of the two fixed points p and q by adjusting the frequency ratio γ. According to equation (21), one has

$$\frac{1}{\left(-\lambda_p^2+1\right)+\mu} = -\frac{1}{\left(-\lambda_q^2+1\right)+\mu}. \tag{23}$$

By substituting equation (22) into equation (23), the optimal frequency ratio can be determined as

$$\gamma_{\text{opt}} = \sqrt{\frac{1+\mu}{\frac{C}{C_n}+\frac{C}{C+\mathbb{C}_s+\mathbb{C}_p}}}. \tag{24}$$

Variations of the optimal frequency ratio γ_{opt} with μ and $\frac{C_n}{C+\mathbb{C}_s+\mathbb{C}_p}$ are shown in figure 5. It can be observed that the optimal frequency ratio may be either greater than or less than 1, depending on the value of C_n. When μ is small (which is usually the case for resonant absorbers), the value of $\gamma_{\text{opt}} \times \sqrt{\frac{C}{C_n}+\frac{C}{C+\mathbb{C}_s+\mathbb{C}_p}}$ is very close to 1.

Subsequently, the optimal damping ratio can be determined by making the response of these two fixed points the peak values, i.e.

$$\frac{\partial\left(H_i(s)K_i\right)^2}{\partial\lambda^2} = 0. \tag{25}$$

Two damping ratios ξ_p and ξ_q can then be derived by substituting equation (22) into equation (25), which however cannot be satisfied simultaneously. In practice, one can use their RMS value as the optimal damping ratio as

$$\xi_{\text{opt}} = \sqrt{\frac{\xi_p^2+\xi_q^2}{2}}. \tag{26}$$

Analytical expression of the optimal damping ratio can then be derived through this equation,

$$\xi_{\text{opt}} = \sqrt{\begin{array}{l}\dfrac{-\mu\left(C_r-C_e\right)\left(-C_r\mu+\mu C_e+\sqrt{2}C_e\alpha\right)+2\sqrt{-\mu^3\left(C_r-C_e\right)^3\left(-C_r\mu+3\mu C_e+2\sqrt{2}C_e\alpha+2C_e\right)}}{32\mu\left(\mu+1\right)\left(C_e-C_r\right)+8\sqrt{2}\alpha\left(3\mu C_e-C_r\mu+2C_e\right)} \\ \dfrac{-\mu\left(C_r-C_e\right)\left(C_r\mu-\mu C_e+\sqrt{2}C_e\alpha\right)+2\sqrt{\mu^3\left(C_r-C_e\right)^3\left(C_r\mu-3\mu C_e+2\sqrt{2}C_e\alpha-2C_e\right)}}{32\mu\left(\mu+1\right)\left(C_r-C_e\right)+8\sqrt{2}\alpha\left(3\mu C_e-C_r\mu+2C_e\right)}\end{array}} \tag{27}$$

where

$$\begin{aligned} C_r &= \frac{C}{C_n} \\ C_e &= C_r + \frac{C}{C+\mathbb{C}_s+\mathbb{C}_p} \\ \alpha &= \sqrt{\frac{\mu\left(C_e-C_r\right)\left(\mu+1\right)}{C_e}}. \end{aligned} \tag{28}$$

Variations of the optimal damping ratio ξ_{opt} with μ and $\frac{C_n}{C+\mathbb{C}_s+\mathbb{C}_p}$ are presented in figure 6. It can be observed that the optimal damping ratio approaches zero as μ becomes small.

2.3. Customization of vibration control

The average power spectral density of the structural displacement can be expressed as:

$$\mathbf{S_{XX}} = \frac{\mathbf{X}^H\mathbf{X}}{N_{\text{dim}}}, \tag{29}$$

where N_{dim} is the number of the measurement/estimation points.

Substituting equation (2) into equation (29) yields:

$$\mathbf{S_{XX}} = \frac{\mathbf{V}\boldsymbol{\Sigma}^H\mathbf{M}\boldsymbol{\Sigma}\mathbf{V}^H}{m}, \tag{30}$$

where

$$\mathbf{M} = \Delta S m_s \mathbf{U}^H\mathbf{U}, m = \Delta S m_s N_{\text{dim}}, \tag{31}$$

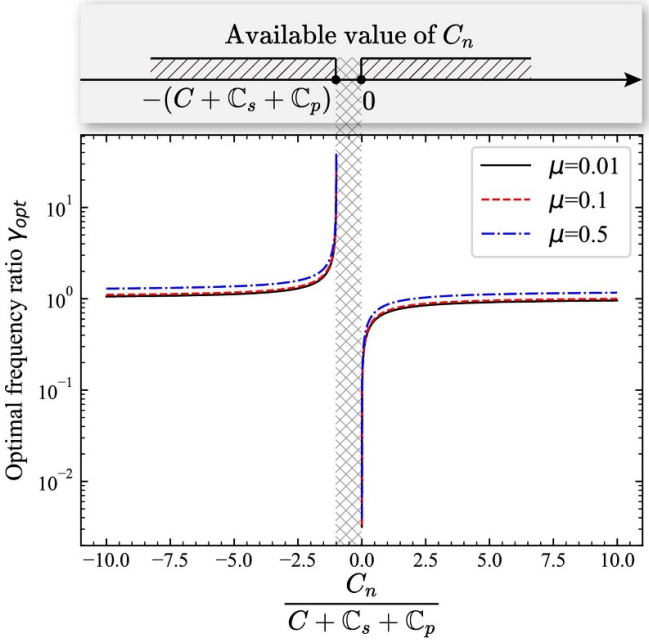

Figure 5. Variation of optimal frequency ratio γ_{opt} with μ and $\frac{C_n}{C+\mathbb{C}_s+\mathbb{C}_p}$.

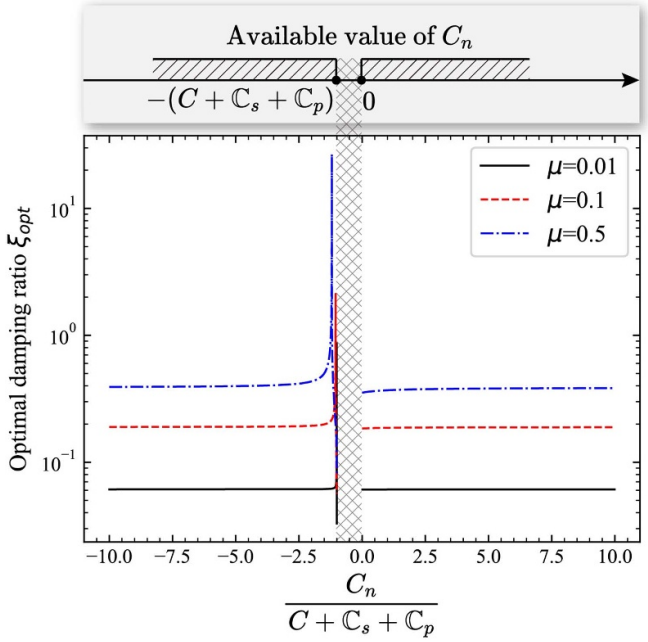

Figure 6. Variation of optimal damping ratio ξ_{opt} with μ and $\frac{C_n}{C+\mathbb{C}_s+\mathbb{C}_p}$.

in which m_s is the normalized mass [32]; ΔS denotes the surface area of the sampling unit as shown in figure 7 m represents the total mass of the primary structure.

Equation (30) can be reformulated for the ith EDRB's resonant response as

$$S_i = \frac{\eta_i^2 M_i}{m}, \tag{32}$$

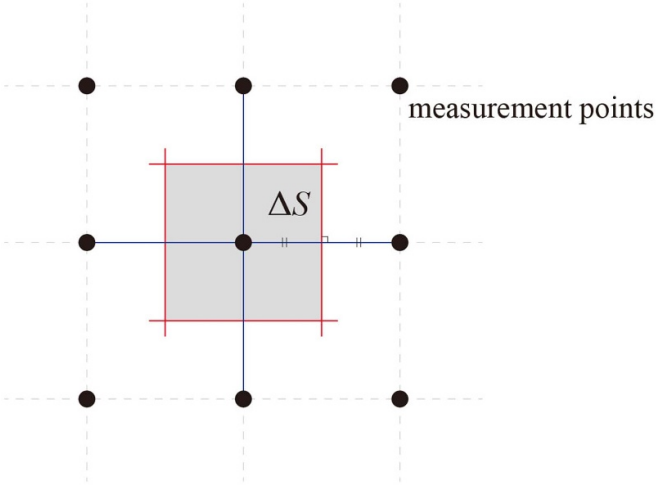

Figure 7. Surface area of a sampling unit.

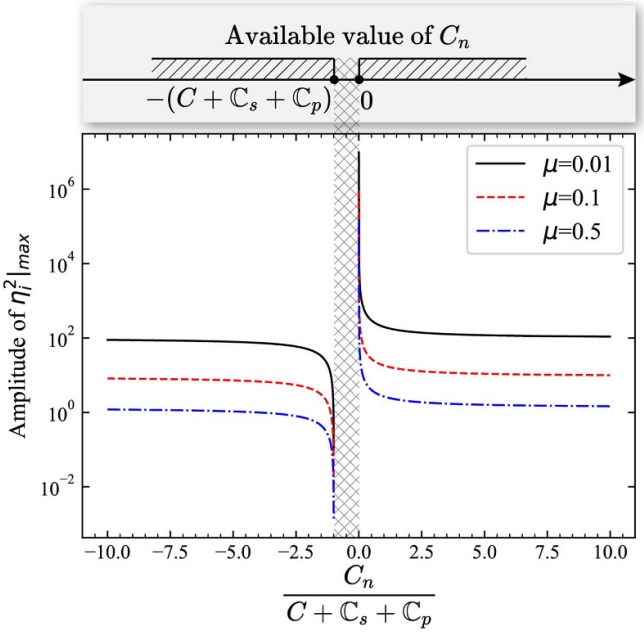

Figure 8. Variation of maximum amplitude $\eta_i^2|_{\text{max}}$ with μ and $\frac{C_n}{C+\mathbb{C}_s+\mathbb{C}_p}$.

where η_i represents the ith element of vector $\boldsymbol{\eta}$. According to equation (19), the maximum normalized magnitude is given by

$$H_i(s)K_i|_{\max} = \frac{1}{\left(-\lambda_p^2+1\right)+\mu}. \tag{33}$$

By substituting equations (22) and (24) into the above equation, the maximum response can be expressed as

$$\eta_i^2|_{\max} = \frac{2F_i^2\left(C+\mathbb{C}_s+\mathbb{C}_p+C_n\right)}{K_i^2\mu\left[1+\mu\right]C_n}. \tag{34}$$

Variations of $\eta_i^2|_{\text{max}}$ with μ and $\frac{C_n}{C+\mathbb{C}_s+\mathbb{C}_p}$ are shown in figure 8, which shows that the improved vibration control performance can be achieved by:

(a) increasing μ of the PZT patch. As indicated by equation (20), μ is influenced by the coupling factor ϑ_i, the inherent capacitance C, and the shunt circuit's residual effect $\mathbb{C}_s$. Consequently, this entails the following design strategies: (a1) employing a larger PZT patch to strengthen the coupling; (a2) choosing a patch with small inherent capacitance; (a3) Incorporating a negative capacitance into the shunt circuit (in series or parallel) to decrease $\mathbb{C}_s$ (refer to table 7 in appendix B for more details).
(b) utilizing a negative capacitance C_n. As shown in figure 8, a negative C_n can always outperform positive capacitance in terms of control performance, which however requires external power. To achieve fully passive control, a positive capacitance with a larger value can be employed to improve the performance while avoiding the need for active components.

We now discuss how to achieve a pre-defined control target. Assuming that the absorber is designed to achieve $S_i|_{\max} = T_i$. According to equations (32) and (34), one has

$$S_i = \frac{M_i}{m}\frac{2F_i^2(s)\left(C+\mathbb{C}_s+\mathbb{C}_p+C_n\right)}{K_i^2\mu\left[1+\mu\right]C_n} = T_i, \tag{35}$$

in which the unknown parameter $F_i(s)$ can be determined through the following optimization process,

$$\arg\min_{F_i(s)} \left\| \eta_i(s) - \frac{F_i(s)}{s^2M_i+K_i} \right\|_2. \tag{36}$$

Substituting equation (36) into equation (35), the analytical expression for the capacitance can be derived to achieve the prescribed vibration reduction level as

$$C_n = \frac{C+\mathbb{C}_s+\mathbb{C}_p}{\dfrac{T_iK_i^2}{2F_i^2(s)M_i/m}\mu(\mu+1)-1}. \tag{37}$$

It should be noted that the expression of capacitance explicitly includes the generalized force term $F_i(s)$, identified based on the measured response data. As such, the proposed design method is not restricted to specific excitation conditions, but remains valid under arbitrary excitation scenarios.

In summary, the shunt absorber design procedure for customized response control is as follows:

1. Extract the EDRB shapes: Measure or numerically simulate the structural response before attaching the PZT patch. Apply SVD to the response data to extract the spatial shapes of the EDRB.
2. Determine patch placement: Use the extracted EDRB shapes to identify an attachment location for the PZT patch, ensuring strong electromechanical coupling.
3. Identify the generalized force $F_i(s)$: After mounting the patch, measure the system's frequency response under short-circuit conditions. Analyze the response using equations (2) and (36) to identify the generalized force $F_i(s)$.
4. Determine the electromechanical coupling coefficient θ: Re-measure the response under open-circuit conditions and compute θ based on the shift in resonant frequencies relative to the short-circuit case, following the method in [39].
5. Design shunt capacitance C_n: Employ equation (37) to calculate the required shunt capacitance values that achieve the desired vibration suppression performance.
6. Compute optimal inductance and resistance: Substitute the derived C_n into equations (24) and (27) to obtain the optimal frequency ratio and damping ratio, from which the corresponding inductance L_n and resistance R_n can be calculated using equation (14).

3. Numerical simulations and discussions

This section presents two case studies to validate the efficacy of the proposed design methodology. The first one involves a rectangular plate, where a stringent response control requirement is imposed to evaluate the feasibility of the method described in section 2. In the second case, a square plate is used to assess the suitability of the proposed method for systems with symmetric modes and its capability to achieve all-equal-peak response control.

3.1. Case 1: customized vibration control of a rectangular plate

In this case, a simply supported aluminum plate with dimensions of 500 × 200 × 1 mm is employed to numerically demonstrate the effectiveness of the proposed design methodology. A unit point force is applied to the structure at the location (10 mm, 10 mm), measured from the plate corner. A PZT patch is attached at the center of the plate, with its geometric dimensions and material properties provided in table 1. Since in this case, the material properties and geometric parameters of the PZT patch are known *a priori*, the electromechanical coupling coefficient θ can be computed analytically using the method described in [18].

Assume the objective is to design the absorber so that the maximum displacement amplitude of the 1st peak is limited to 10 dB (with dB defined in equation (38)), and of the 3rd peak to 30 dB. This control target requires the consideration of the strong coupling between different degrees of freedom in the shunt circuit, making it a good case to demonstrate whether the proposed design method can effectively apprehend such coupling in the absorber design. Notably, the second peak cannot be affected because of the central location of the PZT patch. Let us define

$$\mathrm{PSD}_{\mathrm{dB}} = 10\log_{10}\frac{\mathrm{PSD}}{P_{\mathrm{ref}}^2}, \tag{38}$$

in which $P_{\mathrm{ref}} = 2\times10^{-5}\mathrm{m}^2\,\mathrm{Hz}^{-1}$.

According to equation (37), achieving the desired vibration control requires the determination of the generalized force $F_i(s)$, which can be identified from the measured response

Table 1. Geometric dimensions and material properties of piezoelectric patch.

Parameter	Value
Length	$l = 10$ mm
Width	$w = 10$ mm
Thickness	$h = 1$ mm
Young's modulus	$Y = 5 \times 10^{10}$ N m^{-2}
Poisson ratio	$v = 0.35$
Strain/charge constants	$d_{31} = d_{32} = -190 \times 10^{-12}$ m V^{-1}
Permittivity	$\varepsilon_0 = 8.9 \times 10^{-12}$ Fm^{-1}
Relative dielectric constant	$K_{33}^{\mathrm{T}} = 1200$
Capacitance	$C = \dfrac{K_{33}^{\mathrm{T}} \varepsilon_0 lw}{h} = 1.06 \times 10^{-9}$ F

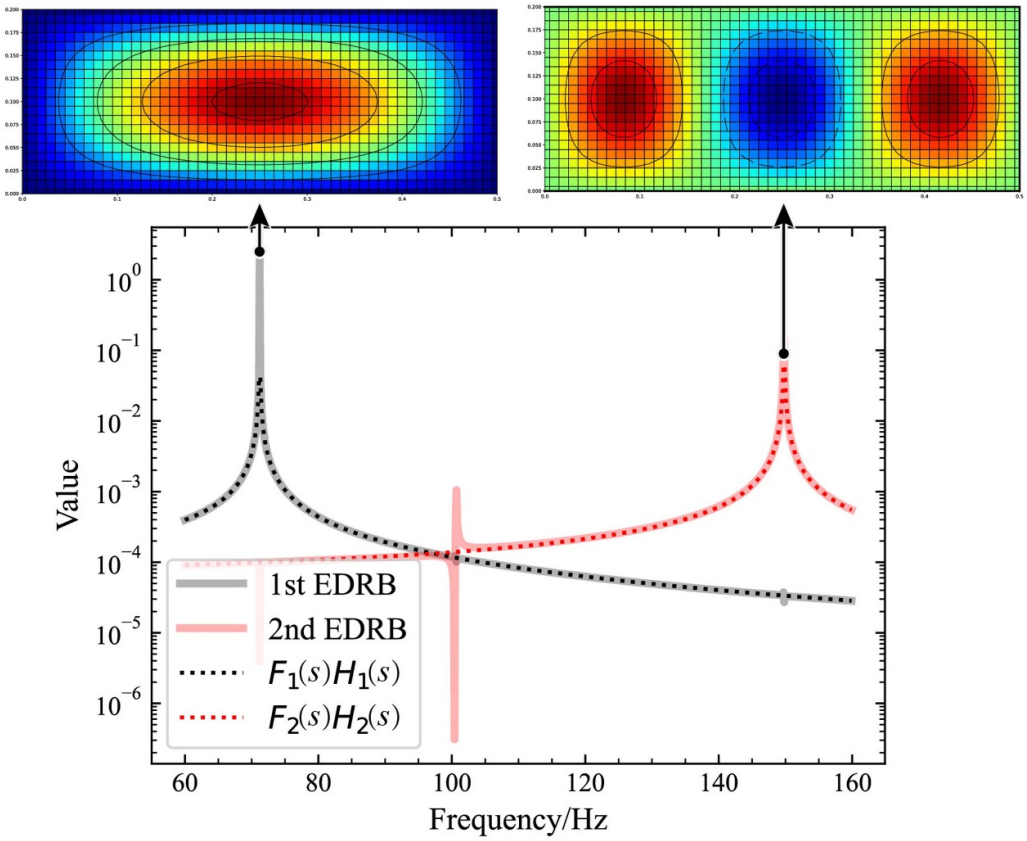

Figure 9. Generalized coordinates of the two targeted EDRBs as defined by **V** in equation (2). The *y*-axis represents the values of the corresponding singular vectors.

using equation (36). Figure 9 shows that the curve of $F_i(s) \times H_i(s)$ closely matches the curve of η_i around resonant frequency, indicating that the identified $F_i(s)$ effectively capture the structural resonant response. The presence of the anti-resonance followed by the resonance arises from the numerical decomposition process inherent to the SVD algorithm.

The optimal frequencies and damping ratios can then be obtained using equations (24) and (27), as tabulated in table 2.

It should be noted that the shunt absorber frequency defined in equation (14) differs from the true resonant frequency observed when the absorber is coupled with the PZT structure. As given by equation (15), the coupled resonant frequency of the absorber is equal to $\omega_n^2 \left(\frac{C}{C_n} + \frac{C}{C+R_s+R_p} \right)$, which is affected by the coupling introduced through the residual degrees of freedom of both the primary system (as represented by $\mathbb{C}_p$) and the shunt circuit (as represented by $\mathbb{C}_s$). Therefore, the observation that the frequency of the 2nd absorber in table 2 deviates from the targeted peak frequency indicates that this control requirement indeed creates a strong coupling condition for the shunt absorber.

The overall structural response (represented by the displacement power spectral density, calculated using equation (29) for 50×20 uniformly distributed measurement points) of the primary structure before and after connecting the shunt circuit is shown in figure 10. It shows that the maximum amplitude of the 1st resonant peak is indeed reduced

Table 2. Optimal parameters of piezoelectric shunt absorbers.

	Capacitance/C_n	Inductance/L_n	Resistance/R_n	Frequency/ω_n	Damping ratio/ξ_n
1st absorber	2.2×10^{-9} F	6.2×10^{3} H	2.7×10^{5} Ω	62.2 Hz	0.057
2nd absorber	2.5×10^{-12} F	4.4×10^{5} H	2.8×10^{6} Ω	7.3 Hz	0.068

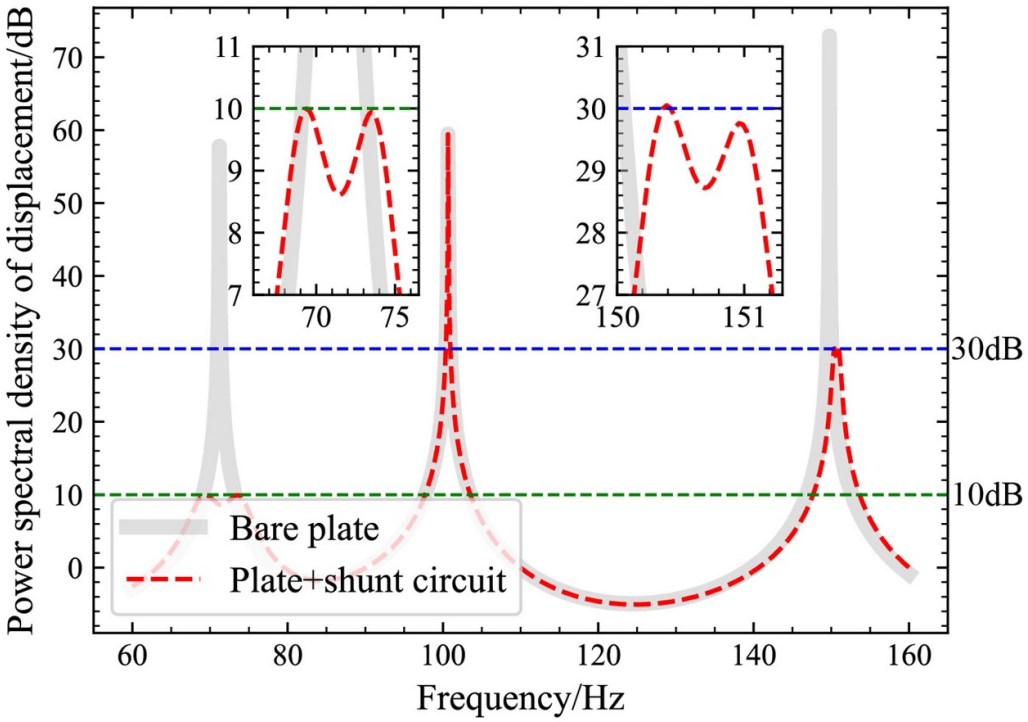

Figure 10. Power spectral density displacement of structure. Response before connecting the shunt circuit is labeled as 'Bare plate', while response after connecting the shunt circuit is labeled as 'Plate + shunt circuit'.

to approximately 10 dB, and that of the 3rd resonant peak roughly down to 30 dB. This demonstrates the effectiveness of the proposed method and highlights its capability to achieve customized vibration control. Additionally, equal peak amplitudes are observed around each controlled peak, indicating that the proposed method effectively incorporates the complex coupling effects into the absorber design.

The proposed design method, based on undamped systems, is re-evaluated for damped systems by using a plate with varying damping ratios (figure 11). It can be seen that the method remains effective for lightly damped structures (damping ratio $\xi < 1\%$). For highly damped systems, vibrational energy is inherently dissipated to a significant extent, resulting in less pronounced resonant responses, thus reducing the necessity of using passive shunt absorbers.

3.2. Case 2: customized all-equal-peak vibration control of a square plate

This numerical case investigates a simply supported square plate with dimensions of 500 × 500 × 1 mm, subjected to a point force applied at (125 mm, 125 mm), measured from the plate corner. A PZT patch, 30 × 30 × 1 mm, is bonded again to the center of the plate, with the same material parameters as the ones used in section 3.1, tabulated in table 1.

The control objective for this case is to achieve an all-equal-peak response across the targeted frequencies, with each peak amplitude reduced to 40 dB. Similar to Case 1, the generalized force $F_i(s)$ should first be identified. The response of the plate is numerically simulated and subsequently decomposed using equation (2), followed by numerical optimization, as shown in equation (36) to calculate the generalized force. Figure 12 demonstrates that the identified generalized force again well characterizes resonant response of square plate with symmetric modes.

Optimal frequencies and damping ratios are then determined using equations (24) and (27), yielding the final results listed in table 3.

The overall response (represented by the displacement power spectral density, calculated using equation (29) for 50 × 50 uniformly distributed measurement points) of the primary structure before and after connecting the shunt circuit is shown in figure 13. The results demonstrate that the two targeted resonant peaks have been effectively attenuated to the pre-defined vibration level of 40 dB, which validates the effectiveness of the proposed method for structures with

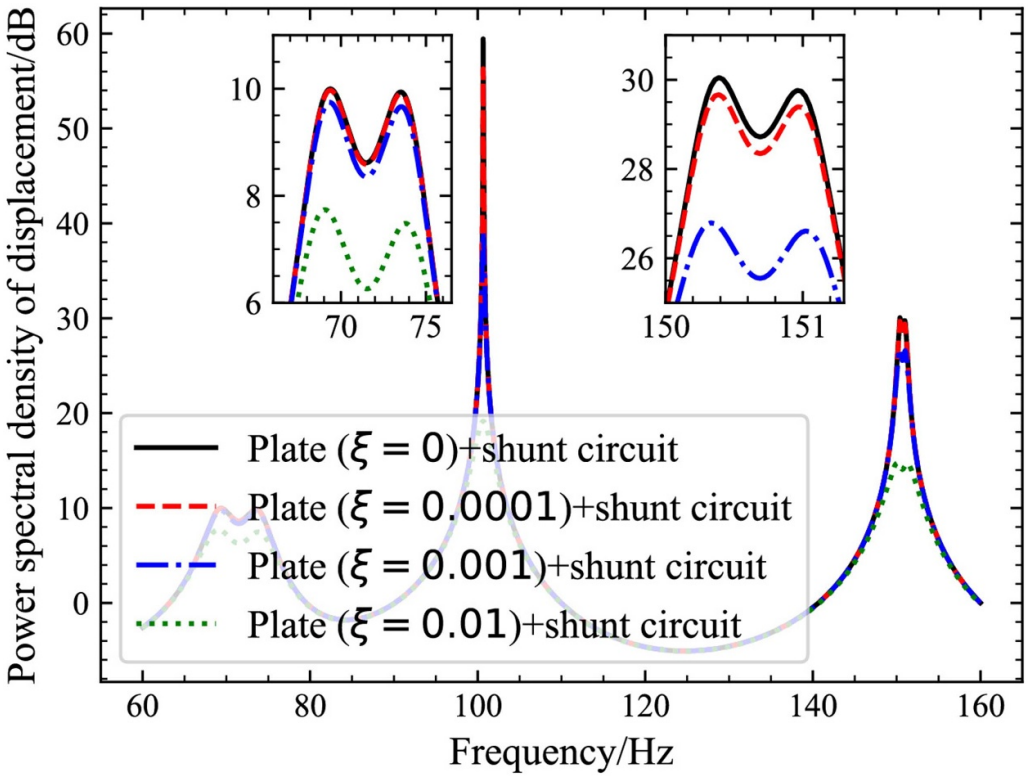

Figure 11. Power spectral density displacement of structure for different damping ratios.

symmetric modes and its capability to achieve an all-equal-peak response design.

4. Experimental validations

This section presents the experimental setup and the testing results to validate the efficacy of the proposed absorber design methodology. As illustrated in figure 14, a square stainless steel plate of 500 × 500 × 1 mm with clamped boundary conditions was tested. Nine small PZT patches, each measuring 45 × 45 × 2 mm, were electrically connected in parallel to form one single PZT patch. The plate was excited using an electrodynamic shaker and a force transducer was used to measure the applied force. Response of this system was collected using a laser vibrometer (PSV 500).

Instead of using analog electrical components such as resistors, inductors, and capacitors, the designed shunt admittance was emulated using dSPACE for experimental convenience. The analog circuit [12, 21], used to interface the dSPACE system with the PZT patch, is shown in figure 15 (see appendix C for more details).

Resistor values used in the circuit (figure 15) are given in table 4.

As discussed in section 2, determining the optimal values of the shunt absorbers requires prior identification of two parameters: the coupling coefficient θ and the generalized force $F_i(s)$. The electromechanical coupling coefficient θ was determined from the shift in resonant frequencies measured under short-circuit and open-circuit conditions of the PZT patch [39]. The measurement using laser vibrometer (PSV-500) gave the corresponding results shown in figure 16.

The resonant frequencies of the plate under short-circuit (f_{sc}) and open-circuit (f_{oc}) conditions are presented in table 5.

The generalized force $F_i(s)$ was then determined by optimizing equation (36). It should be noted that equation (36) assumes an undamped primary system, while experimental data include unavoidable structural damping. Therefore, direct fitting across all frequencies may introduce bias near the resonance peaks. To alleviate this, the identification algorithm avoids the narrow resonance regions and focuses on the rest of the curve where the undamped model provides a sufficiently accurate approximation. To verify the correctness of this optimization, the resulting $F_i(s)H_i(s)$ is compared with $V_i(s)$, which corresponds to the ith column of $\mathbf{V}(s)$ derived from equation (2). As shown in figure 17, the generalized force $F_1(s)$ accurately portraits the resonant behavior near 30 Hz, while $F_2(s)$ fails to well match the frequency distribution of the 2nd EDRB. This is because, as shown in figure 16, the structural response around 117 Hz is low in amplitude, which hinders the accurate extraction of the EDRB during the SVD operation on the measured response performed using equation (2).

Once the control requirement was defined, the capacitance values can be determined by substituting the identified

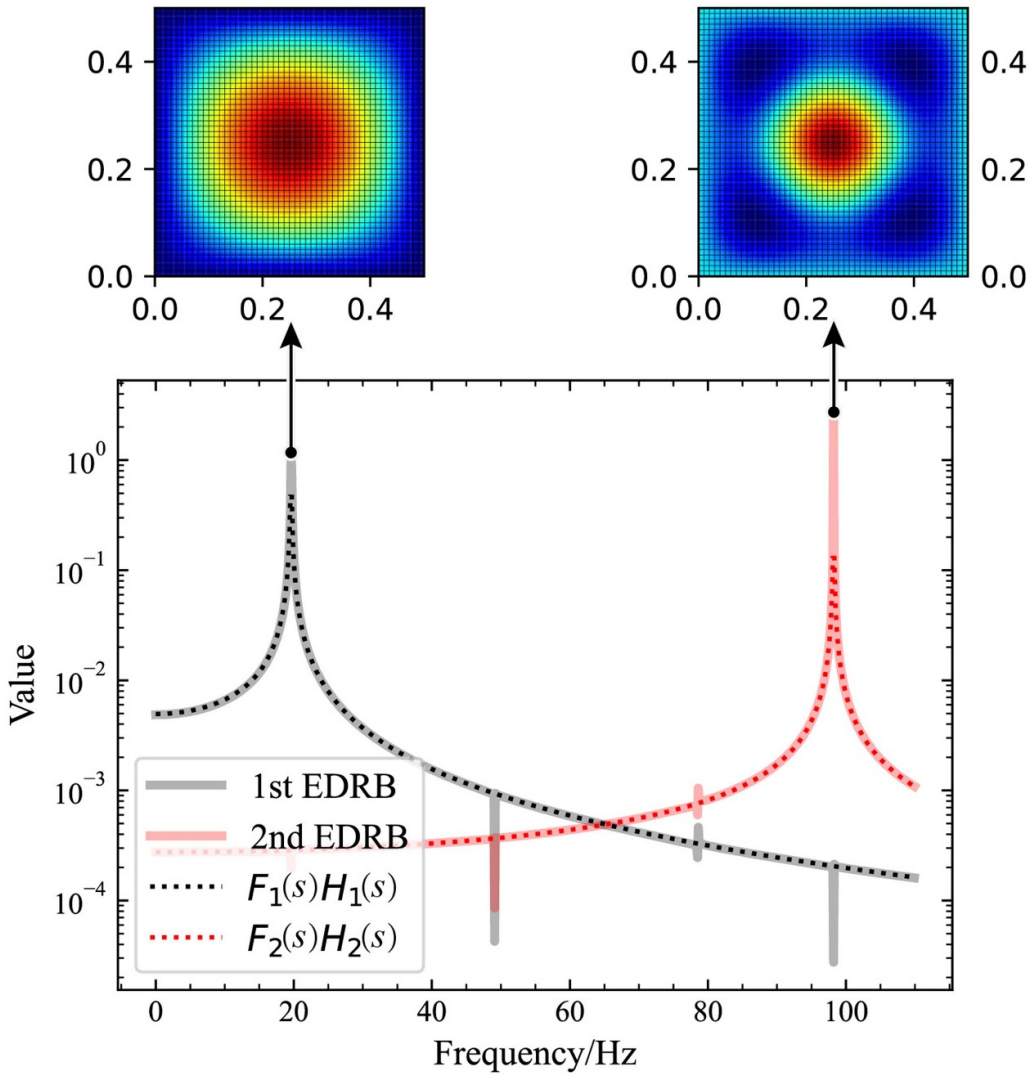

Figure 12. Generalized coordinates of the two targeted EDRBs as defined by **V** in equation (2). The *y*-axis represents the values of the corresponding singular vectors.

Table 3. Optimal parameters of piezoelectric shunt absorbers.

	Capacitance/C_n	Frequency/ω_n	Damping ratio/ξ_n
1st absorber	2.6×10^{-9} F	9.6 Hz	0.085
2nd absorber	3.3×10^{-12} F	1.9 Hz	0.122

parameters into equation (37). The optimal frequencies and damping ratios of the shunt absorber were then obtained using equations (24) and (27), respectively. Since a digital circuit was used to emulate the transfer function of the analog resonant circuit, the parameters (capacitance values, frequencies and damping ratios) obtained in the previous steps need to be updated to compensate for the influence caused by the time delay introduced by the digital processing [40]. This compensation turned out to be particularly important to ensure the accurate design of the shunts. Corresponding details can be found in appendix B.

As illustrated in figure 18, the discretized transfer function implemented in dSPACE matches well with the designed response after being updated according to the correction formulas detailed in appendix B. The updated transfer function was injected into dSPACE, enabling the realization of the desired transfer behavior between V_{ADC} and V_{DAC}, as shown in figure 19.

The overall response (represented by the displacement power spectral density, calculated using equation (29) for 16×16 uniformly distributed measurement points) under two different control targets is presented in figure 20. In the first case, the control objective predefines a response level of 12 dB around 30 Hz and -9 dB around 117 Hz. In the second case, the desired levels are set to 9 dB around 30 Hz and—7 dB around 117 Hz, respectively. These two different control requirements help eliminate experimental

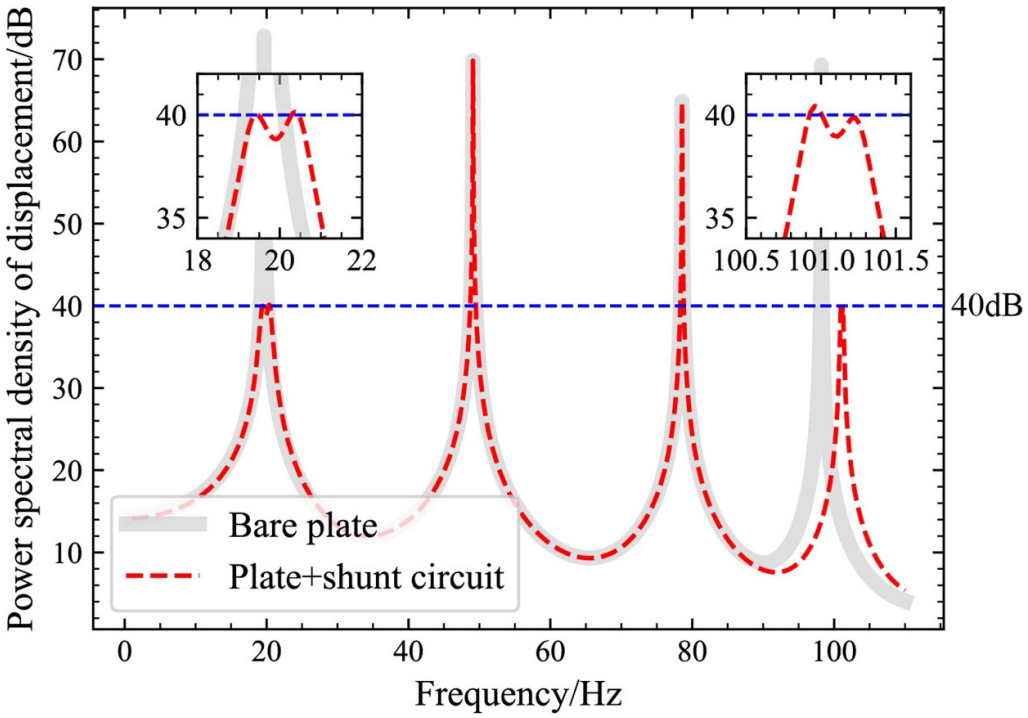

Figure 13. Power spectral density displacement of structure. Response before connecting the shunt circuit is labeled as 'Bare plate', while response after connecting the shunt circuit is labeled as 'Plate + shunt circuit'.

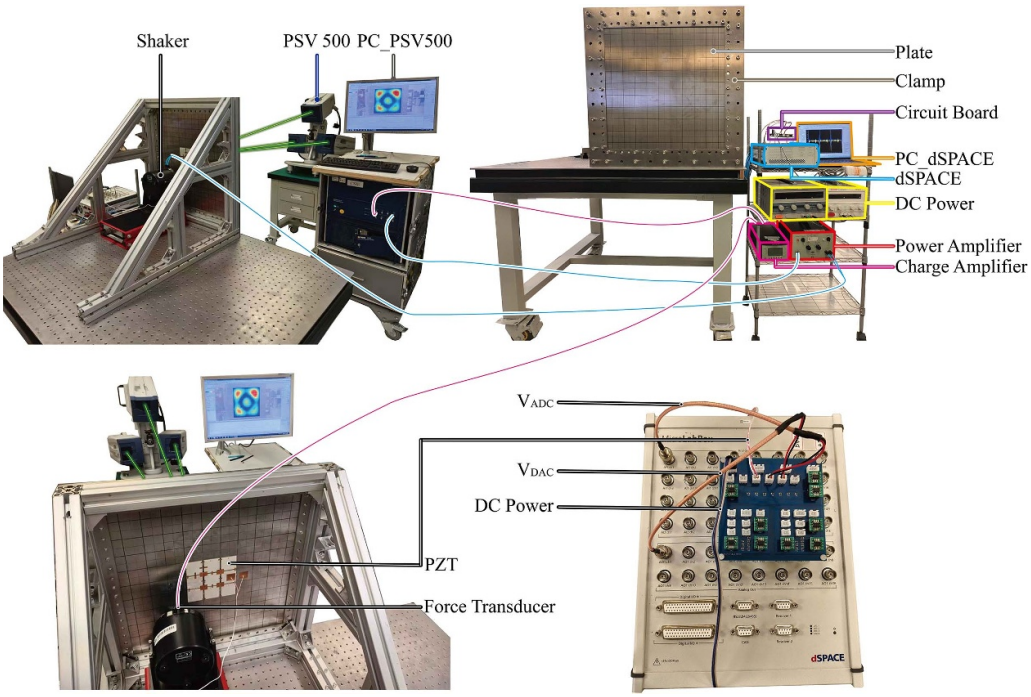

Figure 14. Experimental setup.

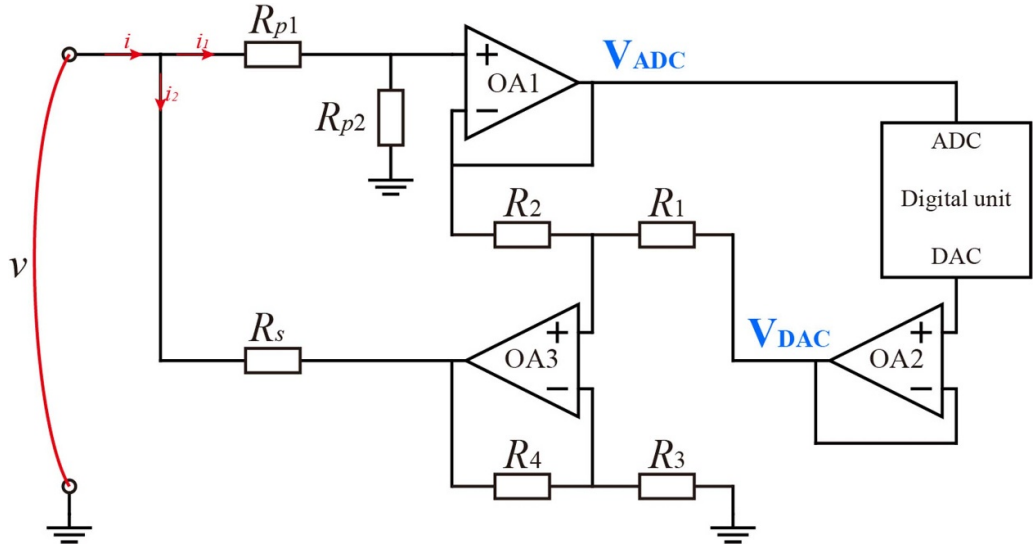

Figure 15. Analog circuit for the interface between dSPACE and the piezoelectric patch.

Table 4. Values of resistors in figure 15.

R_{p1}	R_{p2}	R_1	R_2	R_3	R_4	R_s
50k Ω	50k Ω	10k Ω	10k Ω	10k Ω	50k Ω	50k Ω

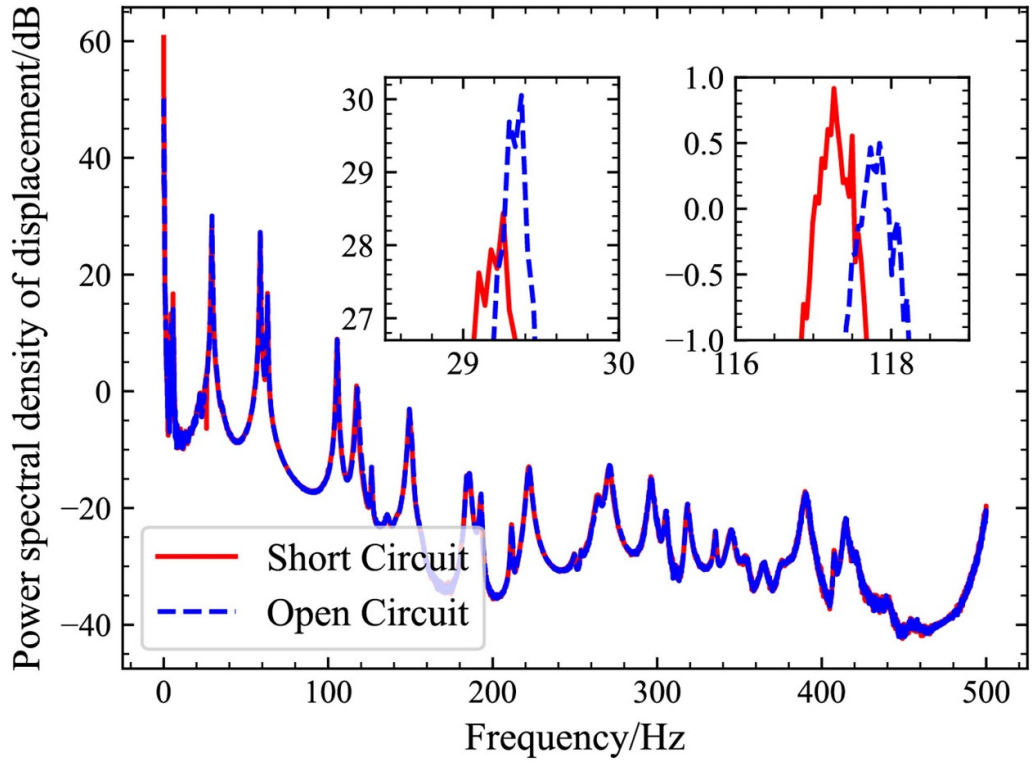

Figure 16. The response of the plate under short-circuit and open-circuit conditions of the shunt circuit.

Table 5. Resonant frequencies under short-circuit and open-circuit conditions.

$f_{sc,1}$	$f_{oc,1}$	$f_{sc,2}$	$f_{oc,2}$	$f_{sc,3}$	$f_{oc,3}$
29.023 Hz	29.063 Hz	117.266 Hz	117.734 Hz	188.789 Hz	190.117 Hz

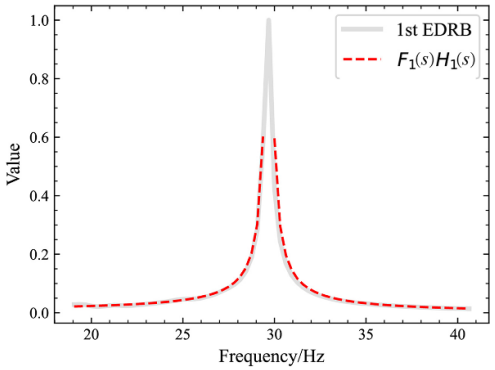

(a1) Generalized coordinate of the 1st EDRB.

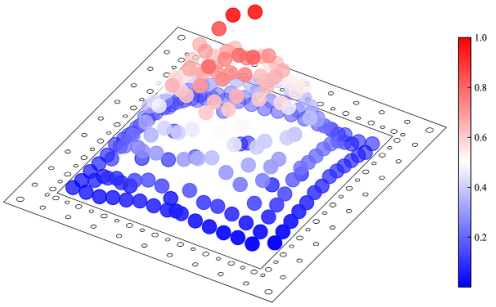

(a2) Vibration shape of 1st EDRB.

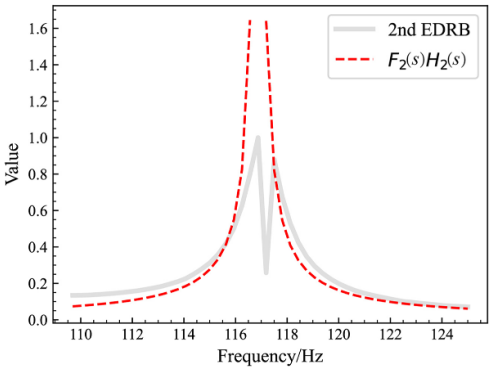

(b1) Generalized coordinate of the 2nd EDRB.

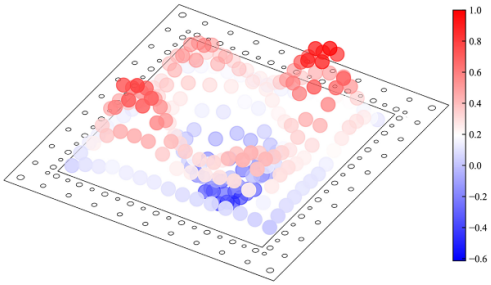

(b2) Vibration shape of 2nd EDRB.

Figure 17. Generalized coordinates and vibration shapes of the two targeted EDRBs as defined by **V** and **U** in equation (2). The *y*-axes in subfigures (a1) and (a2) represent the values of the corresponding singular vectors contained in matrix **V**.

variability and ensure robust validation of the method. The results in figure 20 demonstrate that the proposed design method effectively controls the overall response of the primary structure to meet the pre-specified performance targets, despite some noticeable deviations due to the inaccuracies in the identification of the generalized force and the coupling coefficient. Nevertheless, we believe the ability of the proposed design method in achieving customized vibration reduction target (within the physical limitation of course) is reasonably confirmed through this experimental campaign.

5. Conclusions

In this study, a novel design methodology is proposed to optimize the parameters of a multi-degree-of-freedom shunt circuit feeding a PZT absorber based on the EDRB extracted from the measured structural response of the primary structure. Due to the complex coupling induced by the multiple degrees of freedom of both the primary system and the shunt circuit, two simplifying assumptions are introduced to approximate the continuous PZT structure as an equivalent two-degree-of-freedom mechanical system. This approximation/simplification significantly reduces the complexity of the analysis and the absorber design while approximately preserving the structural-electrical interaction effects taking place inside the coupled system. Based on this simplified model, an inverse approach is proposed to customize the absorber design to achieve pre-defined vibration control target. The validity of the proposed approach is demonstrated through both numerical analyses and experiments. The key conclusions drawn from this work are summarized as follows:

(1) The proposed coupling analysis method and the simplified model effectively capture the salient dynamic features of the PZT structure, offering practical advantages for the design of the shunt absorbers.
(2) The proposed inverse design method provides an efficient framework for achieving customized broadband vibration control. Moreover, the optimization process is computationally straightforward, as the solutions can be directly derived using analytical expressions.
(3) When using dSPACE to emulate the required shunt admittance, system parameters need to be updated to compensate for the effects of time delay introduced by digital processing.

As a final note, a single PZT patch may be insufficient to achieve adequate electromechanical coupling for all structural resonant frequencies. Consequently, the implementation

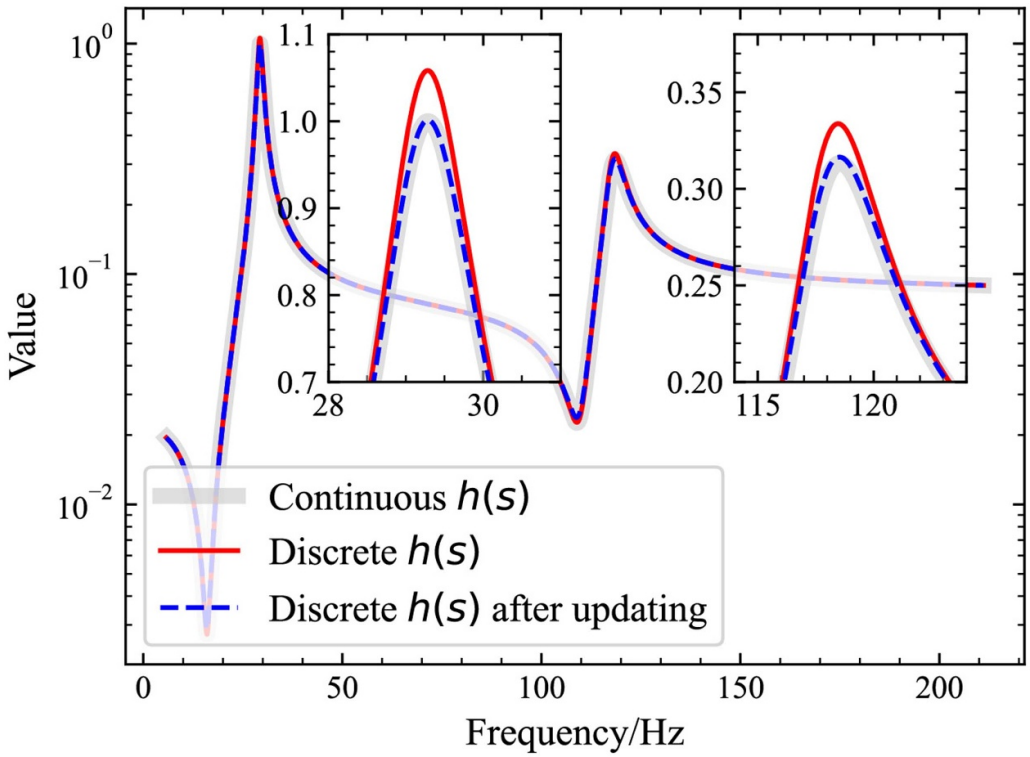

Figure 18. Transfer function value of the attached shunt circuit. Response calculated by equation (13) is labeled as 'Continuous $h(s)$'. After digital processing, the transfer function implemented in dSPACE is labeled as 'Discrete $h(s)$'. When parameters of shunt absorber are updated using the formulas in appendix B, transfer function injected into dSPACE is labeled as 'Discrete $h(s)$ after updating'.

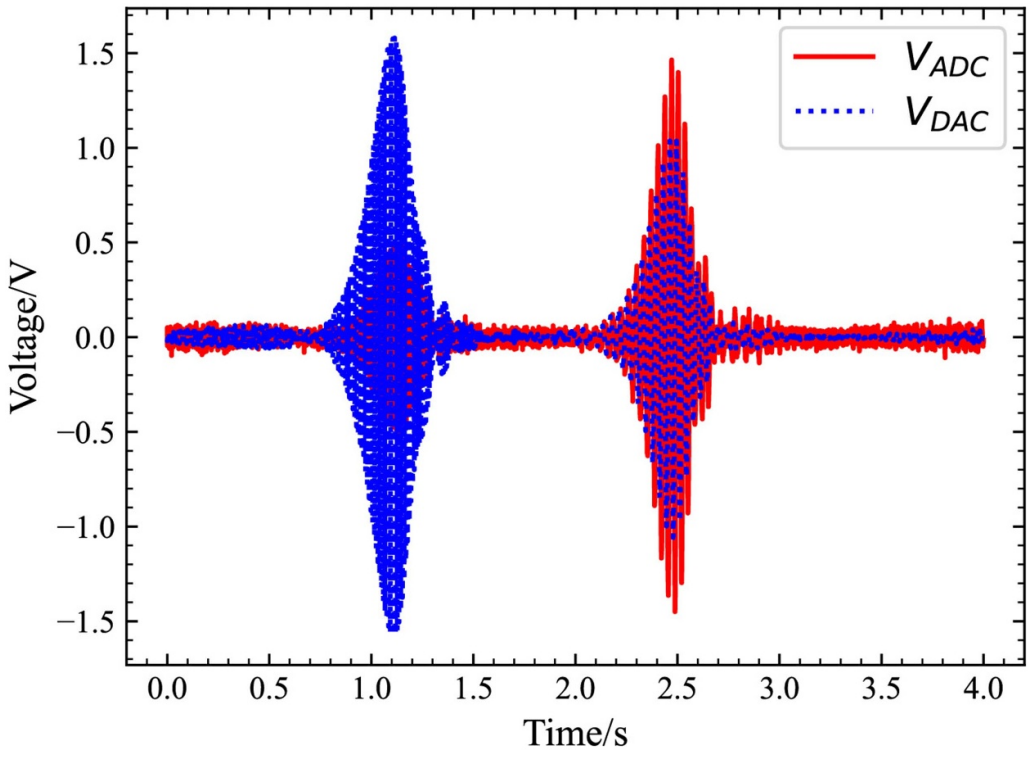

Figure 19. Measured signals of V_{ADC} and V_{DAC}.

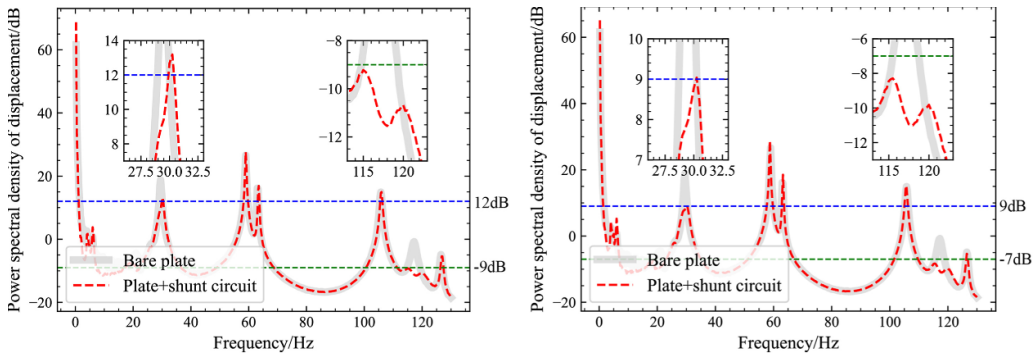

(a) Case 1 (b) Case 2

Figure 20. Power spectral density displacement of structure. Response before connecting the shunt circuit is labeled as 'Bare plate', while response after connecting the shunt circuit is labeled as 'Plate + shunt circuit'.

of multiple PZT patches becomes necessary. This limitation warrants further investigation in future studies.

Data availability statement

All data that support the findings of this study are included within the article (and any supplementary files).

Acknowledgment

The authors gratefully acknowledge Dr Raze Ghislain form University of Liege for his advice on the experiment.

Author contributions

Hangxing Li 0000-0002-7629-5904
Conceptualization (equal), Data curation (equal), Formal analysis (equal), Methodology (equal), Software (equal), Validation (equal), Visualization (equal), Writing – original draft (equal), Writing – review & editing (equal)

Waion Wong 0000-0003-3448-8836
Conceptualization (equal), Funding acquisition (equal), Investigation (equal), Methodology (equal), Project administration (equal), Supervision (equal), Validation (equal), Writing – review & editing (equal)

Li Cheng 0000-0001-6110-8099
Conceptualization (equal), Funding acquisition (equal), Investigation (equal), Methodology (equal), Supervision (equal), Visualization (equal), Writing – original draft (equal), Writing – review & editing (equal)

Appendix A. Modeling of the mechanical model in figure 4

The equation of motion of the structure shown in figure 4 writes

$$\left(s^2 m_1 + k_1\right) x_1 + k_0 \left(x_1 - x_2\right) = f$$

$$k_0 \left(x_1 - x_2\right) - \left(s^2 m_2 + s c_2 + k_2\right) x_2 = 0, \tag{39}$$

where m_1 and k_1 denote the mass and stiffness of the primary system, respectively; m_2, k_2, and c_2 the mass, stiffness, and damping of the absorber, respectively; k_0 the stiffness of the spring connecting the two mass blocks; x_1 and x_2 the displacements of the primary system and the absorber, respectively; and f the external force applied to the primary system. The transfer function of the system can then be derived as:

$$H_1 = \frac{x_1}{f_1} = \frac{1}{s^2 m_1 + k_1 + k_0 \frac{s^2 m_2 + s c_2 + k_2}{s^2 m_2 + s c_2 + k_2 + k_0}}. \tag{40}$$

According to section 2.1, the transfer function of the piezoelectric structure is

$$H_i = \frac{1}{\vartheta_i^2} \frac{1}{s^2 \frac{M_i}{\vartheta_i^2} + \frac{K_i}{\vartheta_i^2} + \frac{1}{C + R_s + R_p} \frac{s^2 L_n + s R_n + \frac{1}{C_n}}{s^2 L_n + s R_n + \frac{1}{C_n} + \frac{1}{C + R_s + R_p}}}. \tag{41}$$

By comparing the two transfer functions, namely equations (40) and (41), it can be observed that the two equations exhibit identical forms when:

$$m_1 = \frac{M_i}{\vartheta_i^2}, \quad k_1 = \frac{K_i}{\vartheta_i^2}, \quad k_0 = \frac{1}{C + R_s + R_p}$$
$$k_2 = \frac{1}{C_n}, \quad m_2 = L_n, \quad c_2 = R_n. \tag{42}$$

Appendix B. Time delay compensation method

When dSPACE is employed to emulate the behavior of an analog circuit, the theoretically derived admittance $\bar{Y}(s)$ deviates from the actual admittance implemented in the dSPACE system, denoted as $Y(s)$. This discrepancy arises from the time delay τ introduced during digital processing, and the two admittance terms are linked by [40]:

$$Y(s) = \bar{Y}(s) \frac{1 - \mathrm{e}^{-\tau s}}{\tau s}. \tag{43}$$

Table 6. Analytical expression for the updated parameters of shunt circuit containing single degree of freedom.

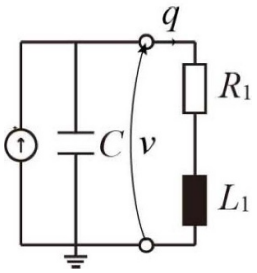	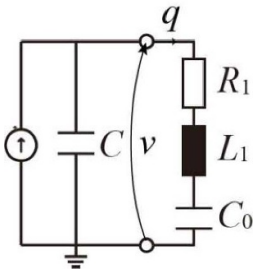	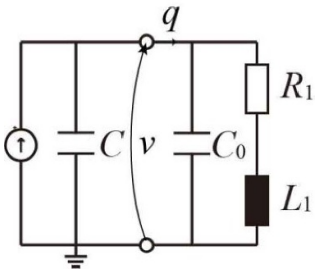
$\begin{cases} \bar{\omega}_1 = \sqrt{\frac{1}{1-\tau\omega_1\xi_1}}\omega_1 \\ \bar{\xi}_1 = \frac{\xi_1+\frac{\tau}{4}\omega_1}{\sqrt{1-\tau\omega_1\xi_1}} \end{cases}$	$\begin{cases} \bar{\omega}_1 = \sqrt{\frac{1}{1-\tau\omega_1\xi_1}}\omega_1 \\ \bar{\xi}_1 = \frac{4\xi_1+\omega_1\tau}{4}\sqrt{\frac{1}{1-\tau\omega_1\xi_1}} \\ \bar{C}_0 = C_0 \end{cases}$	$\begin{cases} \bar{\omega}_1 = \omega_1 \\ \bar{\xi}_1 = \frac{C^2\omega_1\tau+4C^2\xi_1+8CC_1\xi_1+4C_1^2\xi_1}{4C^2-4CC_1\omega_1\tau\xi_1+8CC_1-4C_1^2\omega_1\tau\xi_1+4C_1^2} \\ \bar{C}_0 = C_0 \end{cases}$
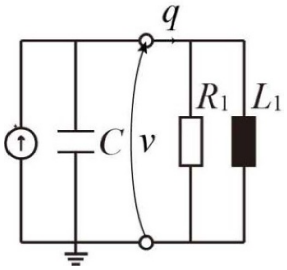	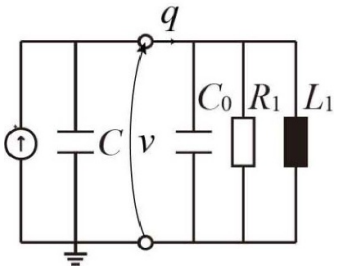	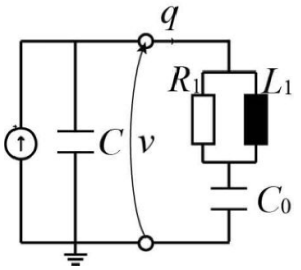
$\begin{cases} \bar{\omega}_1 = \omega_1\sqrt{1-\xi_1\tau\omega_1} \\ \bar{\xi}_1 = \frac{\xi_1+\omega_1\frac{\tau}{4}}{\sqrt{1-\xi_1\tau\omega_1}} \end{cases}$	$\begin{cases} \bar{\omega}_1 = \omega_1\sqrt{1-\frac{\omega_1\xi_1\tau}{1+C_0/C}} \\ \bar{\xi}_1 = \frac{4\xi_1-\frac{\omega_1\tau}{1+C/C_0}+\omega_1\tau}{4\sqrt{1-\frac{\omega_1\xi_1\tau}{1+C_0/C}}} \\ \bar{C}_0 = C_0 \end{cases}$	$\begin{cases} \bar{\omega}_1 = \omega_1 \\ \bar{\xi}_1 = \frac{-4CC_0\xi_1-C_0^2\omega_1\tau-4C_0^2\xi_1}{4C^2\omega_1\tau\xi_1+4CC_0\omega_1\tau\xi_1-4CC_0-4C_0^2} \\ \bar{C}_0 = C_0 \end{cases}$

Expanding the exponential function $e^{-\tau s}$ using Taylor's series expansion gives

$$e^{-\tau s} = 1 + \frac{-\tau s}{1!} + \frac{\tau^2 s^2}{2!} + \ldots. \tag{44}$$

Keeping the first three terms and substituting the resulting expression into equation (43) yield

$$\bar{Y}(s) = \frac{Y(s)}{1-\frac{\tau s}{2}}. \tag{45}$$

By equating the coefficients of different terms of the same order, the updated natural frequency $\bar{\omega}_n$, damping ratio $\bar{\xi}_n$, and capacitance $\bar{C}_n$ can be analytically derived. The results for several commonly used shunt circuits are summarized in tables 6 and 7.

where

$$\omega_1 = \frac{1}{\sqrt{L_1 C}}$$
$$\xi_1 = \begin{cases} \frac{R_1}{2L_1\omega_1} \text{For Series RL Shunt Circuit} \\ \frac{1}{2R_1 C\omega_1} \text{For Parallel RL Shunt Circuit} \end{cases} \tag{46}$$

where

$$B_1 = \begin{cases} \sum_{m=1}^{N} \frac{\omega_m^2 C}{s^2+2s\omega_m\xi_m+\omega_m^2 C/C_m} \text{For Series RLCs Shunt Circuit} \\ \sum_{m=1}^{N} \frac{s^2 C/C_m}{s^2+2s\omega_m\xi_m C/C_m+\omega_m^2 C/C_m} \text{For Parallel RLCs Shunt Circuit} \end{cases}$$
$$B_2 = \begin{cases} \sum_{p=1,p\neq n}^{N} \frac{\omega_p^2 C}{s^2+2s\omega_p\xi_p+\omega_p^2 C/C_p} \text{For Series RLCs Shunt Circuit} \\ \sum_{p=1,p\neq n}^{N} \frac{s^2 C/C_p}{s^2+2s\omega_p\xi_p C/C_p+\omega_p^2 C/C_p} \text{For Parallel RLCs Shunt Circuit} \end{cases} \tag{47}$$

Table 7. Analytical expression for the updated parameters of shunt circuit containing multiple degrees of freedom.

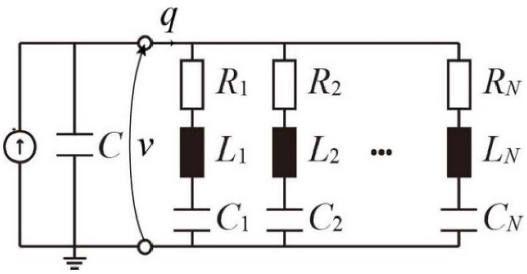	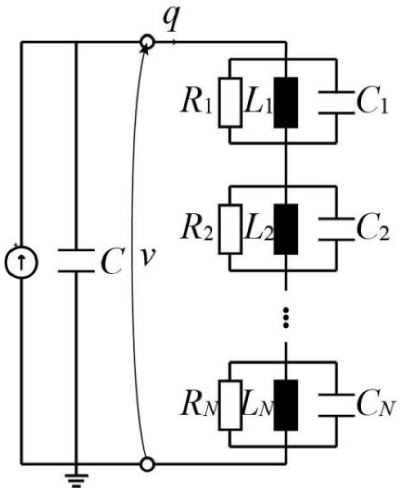
$\bar{\xi}_n = \left\| \frac{\omega_n C/(2s)}{(1+\tau s/2)B_1 - B_2} - \frac{s^2+\omega_n^2 C/C_n}{2s\omega_n} \right\|$	$\bar{\xi}_n = \left\| \frac{s/(2\omega_n)}{(1-\tau s/2)B_1 - B_2} - \frac{s^2 C_n/C+\omega_n^2}{2s\omega_n} \right\|$
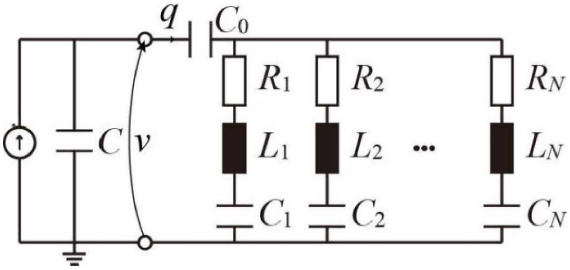	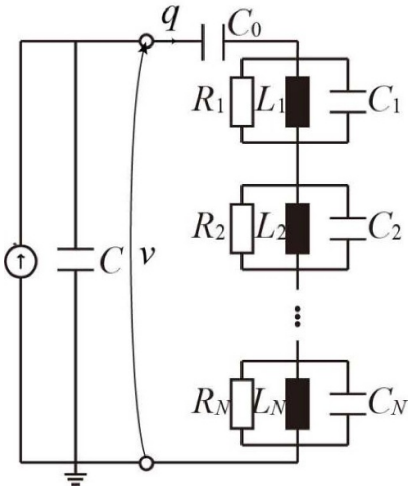
$\bar{\xi}_n = \left\| \frac{\omega_n C/(2s)}{\frac{1}{(1/B_1+1/C_0)(1-\tau s/2)-1/C_0} - B_2} - \frac{s^2+\omega_n^2 C/C_n}{2s\omega_n} \right\|$	$\bar{\xi}_n = \left\| \frac{s/(2\omega_n)}{(B_1+C/C_0)(1-\tau s/2)-C/C_0-B_2} - \frac{s^2 C_n/C+\omega_n^2}{2s\omega_n} \right\|$
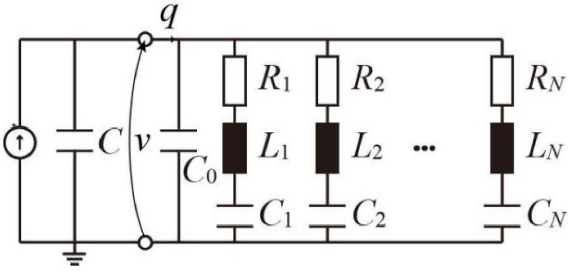	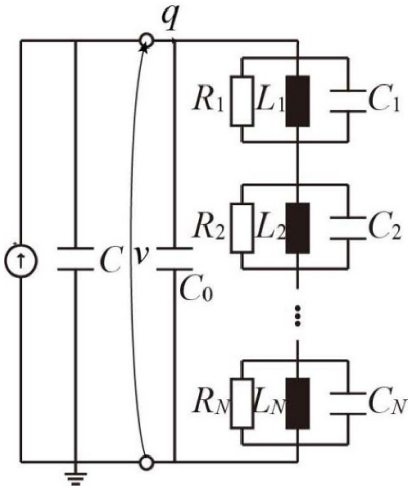
$\bar{\xi}_n = \left\| \frac{\omega_n C/(2s)}{(1+\tau s/2)(C_0+B_1)-C_0-B_2} - \frac{s^2+\omega_n^2 C/C_n}{2s\omega_n} \right\|$	$\bar{\xi}_n = \left\| \frac{s/(2\omega_n)}{\frac{C}{(1+\tau s/2)(C_0+C/B_1)-C_0} - B_2} - \frac{s^2 C_n/C+\omega_n^2}{2s\omega_n} \right\|$

Appendix C. Function of the analog circuit in figure 15

The current i flowing into the piezoelectric patch is given by:

$$i = g_c V_{DAC} + \delta_c \frac{V_{ADC}}{\alpha}, \tag{48}$$

where

$$g_c = \frac{\beta(1-\gamma)}{R_s}, \delta_c = \frac{(\alpha\gamma\beta - 1)(R_{p1} + R_{p2}) - R_s}{R_s(R_{p1} + R_{p2})}$$
$$\alpha = \frac{R_{p2}}{R_{p1} + R_{p2}}, \beta = 1 + \frac{R_4}{R_3}, \gamma = \frac{R_1}{R_1 + R_2}. \tag{49}$$

When the admittance $Y(s)$ is emulated across the two electrodes of the piezoelectric patch, the following expression can be obtained:

$$Y(s) = \frac{i}{V_p} = -g_c \alpha \frac{V_{DAC}}{V_{ADC}} - \delta_c. \tag{50}$$

According to this equation, transfer function of the digital unit can be derived:

$$F(s) = \frac{V_{DAC}}{V_{ADC}} = -\frac{Y(s) + \delta_c}{g_c \alpha}. \tag{51}$$

To fully utilize the operational range of the op-amp, the resistors in figure 15 should be selected such that the output voltage approaches its maximum allowable amplitude.

References

[1] Zhu L, Ma J, Wu Y, Liu F and Kang J 2025 Effects of acoustic environment on sleep and mental health in residential regions near railways *Appl. Acoust.* **227** 110260

[2] Shukla A, Tandel B N and Kajaliya P P 2025 Auditory and mental well-being of teachers in urban noise environment: a partial least square structural equation model approach *Appl. Acoust.* **230** 110417

[3] Escartí-Guillem M S, Garcia-Raffi L M and Hoyas S 2024 Review of launcher lift-off noise prediction and mitigation *Results Eng.* **23** 102679

[4] Ikegame T, Takagi K and Inoue T 2019 Exact solutions to H∞ and H_2 optimizations of passive resonant shunt circuit for electromagnetic or piezoelectric shunt damper *J. Vib. Acoust.* **141** 031015

[5] Paixão J, Foltête E, Sadoulet-Reboul E, Chevallier G and Cogan S 2024 Self-adaptive piezoelectric vibration absorber with semi-passive tunable resonant shunts *J. Sound Vib.* **583** 118424

[6] Gardonio P, Konda Rodrigues G, Dal Bo L and Turco E 2022 Extremum seeking online tuning of a piezoelectric vibration absorber based on the maximisation of the shunt electric power absorption *Mech. Syst. Signal Process.* **176** 109171

[7] Gardonio P and Casagrande D 2017 Shunted piezoelectric patch vibration absorber on two-dimensional thin structures: tuning considerations *J. Sound Vib.* **395** 26–47

[8] Moheimani S R and Fleming A J 2006 *Piezoelectric Transducers for Vibration Control and Damping* (Springer)

[9] Agneni A, Del Sorbo M, Mastroddi F and Polli G M 2006 Multi-modal damping by shunted piezo-patches: possible aeroelastic applications *Int. J. Appl. Electromagn. Mech.* **24** 1–24

[10] Wu S-Y 1998 Method for multiple mode piezoelectric shunting with single PZT transducer for vibration control *J. Intell. Mater. Syst. Struct.* **9** 991–8

[11] Raze G, Paknejad A, Zhao G, Collette C and Kerschen G 2020 Multimodal vibration damping using a simplified current blocking shunt circuit *J. Intell. Mater. Syst. Struct.* **31** 1731–47

[12] Dietrich J, Raze G and Kerschen G 2022 Multimodal shunt damping of mechanical structures using multiple digital vibration absorbers *Eng. Res. Express* **4** 045028

[13] Richardt J D, Lossouarn B, Høgsberg J and Deü J-F 2024 Calibration of multiple shunted piezoelectric transducers with correction for residual modes and shunt interactions *J. Vib. Control.* **31** 24–36

[14] Toftekær J F, Benjeddou A, Høgsberg J and Krenk S 2018 Optimal piezoelectric resistive–inductive shunt damping of plates with residual mode correction *J. Intell. Mater. Syst. Struct.* **29** 3346–70

[15] Raze G, Dietrich J and Kerschen G 2021 Passive control of multiple structural resonances with piezoelectric vibration absorbers *J. Sound Vib.* **515** 116490

[16] Gardonio P, Zientek M and Dal Bo L 2019 Panel with self-tuning shunted piezoelectric patches for broadband flexural vibration control *Mech. Syst. Signal Process.* **134** 106299

[17] Dal Bo L, Gardonio P, Casagrande D E and Saggini S 2019 Smart panel with sweeping and switching piezoelectric patch vibration absorbers: experimental results *Mech. Syst. Signal Process.* **120** 308–25

[18] Casagrande D, Gardonio P and Zilletti M 2017 Smart panel with time-varying shunted piezoelectric patch absorbers for broadband vibration control *J. Sound Vib.* **400** 288–304

[19] Berardengo M, Høgsberg J, Manzoni S, Vanali M, Brandt A and Godi T 2020 LRLC-shunted piezoelectric vibration absorber *J. Sound Vib.* **474** 115268

[20] Zhou S and Bao B 2022 Investigation on high-order resonant electromagnetic shunt dampers for vibration control: methodology and optimum tuning *Struct. Control Health Monit.* **29** e3094

[21] Raze G, Dietrich J, Lossouarn B and Kerschen G 2022 Shunts vs networks: tuning and comparison of centralized and decentralized piezoelectric vibration absorbers *Smart Mater. Struct.* **31** 115006

[22] Raze G, Dietrich J, Lossouarn B and Kerschen G 2022 Modal-based synthesis of passive electrical networks for multimodal piezoelectric damping *Mech. Syst. Signal Process.* **176** 109120

[23] Raze G, Jadoul A, Guichaux S, Broun V and Kerschen G 2019 A digital nonlinear piezoelectric tuned vibration absorber *Smart Mater. Struct.* **29** 015007

[24] Wang C, Yao G and Liu M 2024 Passive vibration control of subsonic thin plate via nonlinear capacitance and negative capacitance coupled piezoelectric shunt damping *Thin Walled Struct.* **198** 111656

[25] Berardengo M, Thomas O, Giraud-Audine C and Manzoni S 2017 Improved shunt damping with two negative capacitances: an efficient alternative to resonant shunt *J. Intell. Mater. Syst. Struct.* **28** 2222–38

[26] Berardengo M, Manzoni S, Thomas O and Vanali M 2018 Piezoelectric resonant shunt enhancement by negative capacitances: optimisation, performance and resonance cancellation *J. Intell. Mater. Syst. Struct.* **29** 2581–606

[27] Zhang L, Li M, Sun X and Cheng W 2024 A nonlinear piezoelectric shunt absorber with tunable piecewise linear negative capacitance *Smart Mater. Struct.* **33** 85037

[28] Gardonio P and Rodrigues G K 2024 Shunted piezoelectric patch adaptive vibration absorber set to maximise electric power absorption: a comparison between parallel and series RL-shunts *J. Vib. Control.* **31** 37–50

[29] Zhang L, Sun X, Dietrich J, Kerschen G and Cheng L 2023 Enhanced energy transfer and multimodal vibration mitigation in an electromechanical acoustic black hole beam *J. Sound Vib.* **561** 117841
[30] Konda Rodrigues G, Gardonio P, Dal Bo L and Turco E 2023 Multimodal vibration control with piezoelectric patches connected to self-tuning RLC shunts *Mech. Adv. Mater. Struct.* **30** 1050–63
[31] Wang X, Wang D, Li F, Zhang Y, Xu Z, Wang T, Fu G and Lu C 2023 Self-learning vibration absorber with negative electromagnetic stiffness for variable vibration *Int. J. Mech. Sci.* **248** 108225
[32] Gardonio P and Turco E 2019 Tuning of vibration absorbers and Helmholtz resonators based on modal density/overlap parameters of distributed mechanical and acoustic systems *J. Sound Vib.* **451** 32–70
[33] Li H, Wu S, Chen Q and Fei Q 2021 Design of dynamic absorbers to control the flexural resonant vibration of structures characterized by multiple natural modes *J. Sound Vib.* **513** 116415
[34] Wu S and Li H 2023 A data-driven design method of distributed dynamic vibration absorber for broadband vibration suppression of thin-walled structures *Thin-Walled Struct.* **182** 110264
[35] Lopes V Jr, Savi M A and Steffen V Jr (eds) 2016 *Dynamics of Smart Systems and Structures: Concepts and Applications* 1st edn (Springer) (https://doi.org/10.1007/978-3-319-29982-2)
[36] Preumont A 2018 *Vibration Control of Active Structures: An Introduction* 4th edn (Springer)
[37] Harville D A 1998 *Matrix Algebra from a Statistician's Perspective* (Taylor & Francis)
[38] Ding J and Zhou A 2007 Eigenvalues of rank-one updated matrices with some applications *Appl. Math. Lett.* **20** 1223–6
[39] Raze G 2021 Piezoelectric digital vibration absorbers for multimodal vibration mitigation of complex mechanical structures *PhD Thesis* ULiège, Université de Liège [Faculty of Applied Sciences], Liège, Belgium
[40] Raze G, Dietrich J and Kerschen G 2022 Onset and stabilization of delay-induced instabilities in piezoelectric digital vibration absorbers *J. Intell. Mater. Syst. Struct.* **33** 2033–48